Greatly enhanced continuous-wave terahertz emission by nano-electrodes in a photoconductive photomixer

H. Tanoto[1], J. H. Teng[1]*, Q. Y. Wu[1], M. Sun[2], Z. N. Chen[2], S. A. Maier[3], B. Wang[1], C. C. Chum[1], G. Y. Si[4], A. J. Danner[4] and S. J. Chua[4]

An efficient, room-temperature-operation continuous-wave terahertz source will greatly benefit compact terahertz system development for high-resolution terahertz spectroscopy and imaging applications. Here, we report highly efficient continuous-wave terahertz emission using nanogap electrodes in a photoconductive antenna-based photomixer. The tip-to-tip nanogap electrode structure provides strong terahertz field enhancement and acts as a nano-antenna to radiate the terahertz wave generated in the active region of the photomixer. In addition, it provides good impedance-matching to the terahertz planar antenna and exhibits a lower RC time constant, allowing more efficient radiation, especially at the higher part of the terahertz spectrum. As a result, the output power of the photomixer with the new nanogap electrode structure in the active region is two orders of magnitude higher than for a photomixer with typical interdigitated electrodes. The terahertz emission bandwidth also increases by a factor of more than two.

Terahertz electromagnetic waves have unique properties such as low photon energy, a fingerprint spectral range for biomolecules, and transparency to several optically opaque materials, such as clothing and paper. Terahertz waves have already found far-reaching applications ranging from molecular spectroscopy to astronomy, environmental monitoring, bio-imaging, security screening and many others[1–6]. Although terahertz science and technology have made significant progress in past decades, there is still a lack of efficient room-temperature-operation continuous-wave (c.w.) terahertz sources, which would greatly benefit many of the aforementioned terahertz applications, especially narrow-bandwidth high-resolution spectroscopy and imaging[5,6].

Quantum cascade lasers (QCLs) are promising semiconductor-based c.w. terahertz sources[7–10]. However, they typically require cryogenic cooling, particularly at the lower terahertz range, and the highest reported operating temperatures without an external magnetic field are 186 K at 3.9 THz and 163 K at 1.8 THz (refs 11,12). One promising technique for realizing c.w. terahertz sources operating at room temperature uses photomixing in ultrafast photoconductive semiconductor materials[13–16]. The efficiency of such devices is determined by the internal efficiency of the semiconductor materials used and the efficiency of the metal planar antenna in radiating the terahertz waves. Currently, the low efficiency of both parts limits the output power of c.w. terahertz photomixers to the microwatt level[17]. Needless to say, improving the efficiency of terahertz photomixing sources has been the subject of intense research efforts, with most focusing on optimization of the photomixer materials and on the design of more efficient terahertz antennas[18–23]. For the past decade, interdigitated electrode structures (originally used in metal–semiconductor–metal (MSM) photodetectors[23]) have been widely used in photomixers to improve the efficiency of photon-to-current conversion. Optimization of the interdigitated electrodes leads to a trade-off between electrode finger separation and photocarrier generation intensity. To achieve higher efficiency, the transit time for photogenerated carriers should be reduced, which requires a reduction in finger electrode separation. However, such a strategy leads to a smaller photoconductive area being exposed to the impinging optical pump laser, and therefore fewer photogenerated carriers. A new design for the active region structure that can circumvent this limitation is desired in order to significantly improve the efficiency of c.w. terahertz photomixers.

Plasmonic metamaterials have provided unique opportunities for manipulating electromagnetic waves in the terahertz range. Many novel terahertz devices have been demonstrated, such as terahertz guiding by spoof surface plasmon polaritions[24–26], frequency agile filters and modulators[27,28], perfect absorbers[29] and collimation of a terahertz QCL beam[30]. Recently it was reported that the terahertz field can be enhanced by orders of magnitude in a metal nanoslit (70 nm) far beyond the skin depth[31]. However, implementation of plasmonic metamaterials to enhance the performance of the most critical and desired c.w. terahertz sources has yet to be demonstrated. In this Article, we report the use of nanogap electrodes as the active region in a photoconductive antenna (PCA)-based c.w. terahertz source to enhance the localized field of both near-infrared light and the terahertz wave. We demonstrate two orders of magnitude enhancement in terahertz emission power compared to a conventional photomixer using interdigitated electrodes.

Experimental results

Semiconductor materials used as PCA-based photomixers must exhibit high resistivity, high carrier mobility and ultrashort carrier lifetime. Low-temperature-grown GaAs (LT GaAs) has been shown to have such characteristics[14–18]. The samples used in our experiment had a 1-μm-thick LT GaAs layer grown on a 1-μm-thick AlAs layer on a semi-insulating GaAs substrate using

[1]Institute of Materials Research and Engineering, Agency for Science, Technology and Research (A*STAR), Singapore 117602, [2]Institute for Infocomm Research, Agency for Science, Technology and Research (A*STAR), Singapore 138642, [3]Department of Physics, Imperial College London, London SW7 2AZ, UK, [4]Department of Electrical and Computer Engineering, National University of Singapore, Singapore 117576. *e-mail: jh-teng@imre.a-star.edu.sg
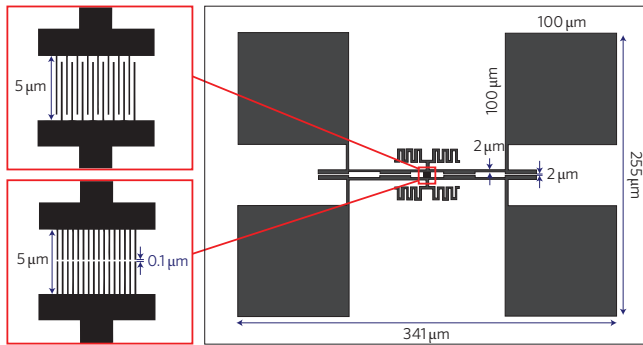
121

Figure 1 | Schematic drawings of the fabricated c.w. terahertz photomixers. Right: overall antenna structure with four bias pads and a modified meander terahertz antenna design. Left: active region designs with interdigitated electrodes (top) and tip-to-tip nanogap electrodes (bottom).

molecular beam epitaxy (MBE). The LT GaAs has a resistivity of $\sim 5 \times 10^7 \Omega$ cm, carrier mobility of $\sim 5,000$ cm^2 V^{-1} s^{-1} and sub-picosecond carrier lifetime. The samples were fabricated into c.w. terahertz photomixers by using photolithography and electron-beam lithography for the patterning of the micro-antenna structure and nano-electrode active region, respectively, followed by electron-beam metal deposition and lift-off. The fabrication process is described in detail in the Supplementary Methods. Schematic drawings and the dimensions of the devices are presented in Fig. 1. The width and separation of the electrode fingers of the active region are 100 nm and 300 nm, respectively, the same for both interdigitated and tip-to-tip nanogap electrodes. Plan-view scanning electron microscopy (SEM) images of the photomixer with interdigitated electrodes and tip-to-tip nanogap electrodes are presented in Fig. 2. Both devices have a modified meander antenna, which has similar effective radiating parts as a simple dipole antenna, but better impedance matching.

The devices were tested at the same d.c. bias voltage of 15 V and excited by two tunable distributed feedback (DFB) lasers. The tunable lasers had central emission wavelengths of 852 nm and 855 nm, respectively, and a total output power of 90 mW. The terahertz wave emitted from the GaAs substrate side was coupled to a silicon hyper-hemispherical lens and measured by vacuum Fourier-transform infrared spectroscopy (FTIR) with a liquid helium-cooled silicon bolometer detector. Details of the measurement set-up are presented in Supplementary Fig. 1. Selected emission spectra of the tip-to-tip nanogap photomixer as recorded by the FTIR system are shown in Fig. 3a. The x-axis is the wavenumber, with 33.33 cm^{-1} approximately equal to 1 THz in frequency. The tip-to-tip nanogap photomixer emission spectra from 7 cm^{-1} to 33 cm^{-1} are presented in the plot. Emissions were actually recorded up to 53 cm^{-1}, but these are not presented due to the large intensity difference with the spectrum below 33 cm^{-1}. The inset of Fig. 3a shows the emission spectra of the interdigitated photomixer; these have a similar shape to that of the tip-to-tip nanogap photomixer, but with much lower intensity. The peak position of the terahertz emission in Fig. 3a is equal to the laser offset. As an example, for a peak position of 11.7 cm^{-1}, the laser offset frequency would be 0.35 THz. The characteristic of a c.w. terahertz photomixer emission, with its very narrow linewidth determined by the linewidth of the pump lasers (<10 MHz in our case), is promising for applications in high-resolution spectroscopy. The recorded emission spectra linewidth is limited by the resolution of the FTIR system (~ 6 GHz). The emission spectrum of a mercury lamp is also included as reference; the mercury lamp has an almost flat broadband emission across the measured range.

To obtain the output power of the c.w. terahertz photomixers, we used the calibration method as described in the Supplementary

Methods. The measured c.w. terahertz emission powers of the photomixer with interdigitated electrodes and tip-to-tip nanogap electrodes are shown in Fig. 3b. Significant enhancement in the output power is observed across a bandwidth of ~ 1.3 THz for the tip-to-tip nanogap electrode photomixer compared to the interdigitated photomixer. The output power of the photomixer with the interdigitated electrode configuration fell below the detection limit at 0.75 THz. However, the photomixer with tip-to-tip electrode configurations emitted even stronger output power at its highest operating frequency of ~ 1.6 THz than the highest peak power from the interdigitated electrode photomixer at ~ 0.3 THz. The total enhancement of the output power was approximately two orders of magnitude across the range. At ~ 400 GHz, the enhancement from the nanogap photomixer was more than three orders of magnitude. These measurement results clearly demonstrate the advantages of using planar terahertz antennas coupled with a tip-to-tip nanogap active region, resulting in highly efficient c.w. terahertz photomixers.

Discussion

When two optical inputs with frequencies f_1 and f_2 are applied to the photomixer, the materials and antenna can respond only up to the lower envelope frequency, which is $|f_1 - f_2|$. An a.c. current with a frequency of $|f_1 - f_2|$ is induced by the movements of photogenerated carriers between the d.c. biased planar metal electrodes on the photomixer materials. The E-field distribution in the near field of the entire structure, including the active photomixing region and the meander antenna, under illumination by a 1 THz plane wave was simulated using CST Microwave Studio. Localized submeshing was used in the photomixer active region or the illuminated electrodes area to enhance the accuracy. The metal electrodes and planar antenna were modelled as perfect electrical conductors (PECs). The results for the tip-to-tip nanogap electrodes photomixer and the conventional interdigitated electrodes photomixer are shown in Fig. 4a,b, respectively. The dimensions used in the simulations were the same as those in Fig. 1.

The E-field (E_0) of the incident terahertz plane wave was kept at 1 V m^{-1} for both structures. From Fig. 4a, it can be seen clearly that the electric field intensity is greatly enhanced within the tip-to-tip nanogap region, predominantly due to a nano-antenna effect, which is similar to the well-known lightning-rod effects[32]. For this
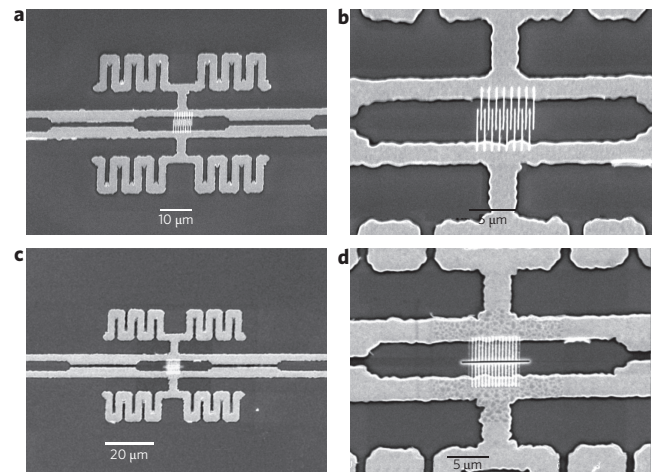

Figure 2 | Plan-view SEM images of the c.w. terahertz photomixers. a, Overall antenna structure with the modified meander terahertz antenna. **b,** Zoom-in of interdigitated electrodes at the active region. **c,** Overall antenna structure of the device with the new active region design. **d,** Zoom-in of tip-to-tip nanogap electrodes at the active region, with the 100 nm gap at the centre defined by FIB milling.
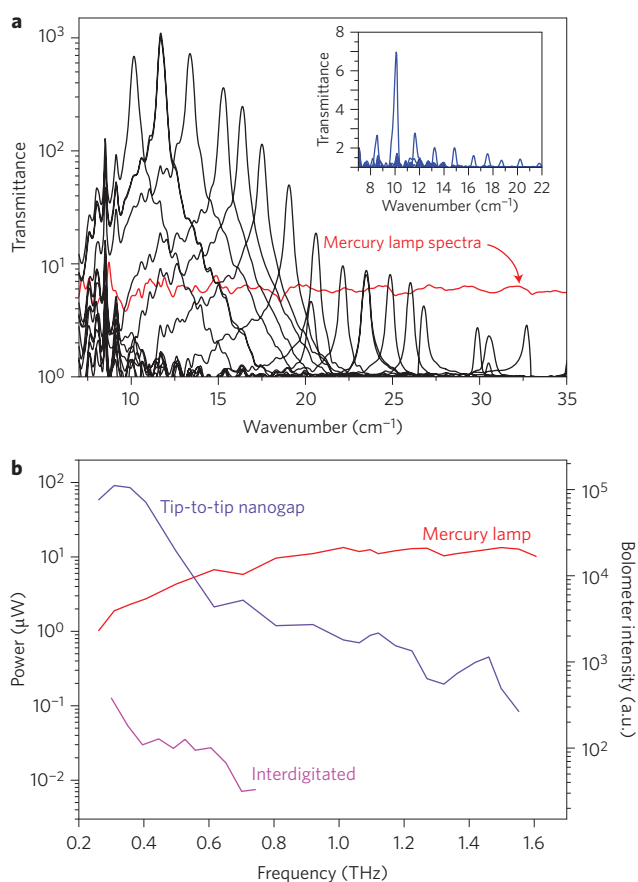
Figure 3 | Terahertz output characteristics of the photomixers. a, Emission spectra of the tip-to-tip nanogap photomixer recorded at different laser offset frequencies. A mercury lamp emission spectrum is included as reference. Inset: emission spectra of the interdigitated photomixer. Note the much lower intensity compared to the tip-to-tip nanogap photomixer. **b**, Output power comparisons of the c.w. terahertz photomixers with interdigitated electrodes and tip-to-tip nanogap electrodes. The output power of a mercury lamp is included as reference.

structure, the E-field of the incident terahertz plane wave was aligned along the y-axis, in accordance with the direction of the electric field under d.c. bias. The lightning-rod-assisted evanescent tunnelling through the subwavelength gap allows the incident terahertz wave arriving on the metal electrode surface to be transmitted more intensely. Owing to the intense E-field at the active region, which is analogous to a current source, the E-field intensity radiated at both arms of the dipole antenna structure is also enhanced. Furthermore, the active region in this case not only acts as a current source, but also contributes to the overall emission of terahertz waves. As for the structure in Fig. 4b, the E-field of the incident terahertz plane wave was chosen to be polarized along the x-axis so as to make it parallel with the dominant direction of the electric field during d.c. bias. The structure exhibits a much lower E-field amplitude. Although enhancement is also present in this configuration, the E-field was not radiated, but was instead trapped in the substrate. Because the interdigitated electrode configuration resembles a series of parallel-plate capacitors, the electromagnetic energy is stored rather than emitted. We tested the polarization of the terahertz wave emitted from both types of photomixer, and the nanogap electrode photomixer indeed showed much stronger vertical (y-axis) polarization than the interdigitated one in the lower terahertz range where the resonance occurred.

As the two-colour optical inputs contain a beat signal oscillating in the terahertz regime and because the width of the electrodes is much smaller than the wavelength, strong electric field localization and confinement should occur for the terahertz wave[31,33–36]. Accordingly, we used finite-difference time-domain (FDTD) simulations to determine the field enhancement factor. A plane wave at a wavelength of 300 μm (~1 THz) was used to illuminate the structure. The dimensions of the device were as presented in Fig. 1, with the gap of the tip-to-tip nano-electrodes being the only variable. Figure 5a shows the field intensity enhancements compared to the interdigitated structure as the gap in the tip-to-tip nanogap electrode structures was varied from 50 nm to 1,000 nm. The field intensity was obtained at the centre of the gap. It was found that the enhancement could be as large as 400× in a 50 nm gap and 100× in a 100 nm gap, the same dimension as used in the test devices. The results are in agreement with those reported by Seo and colleagues[31]. As a comparison, we also calculated the field enhancement factor at 850 nm
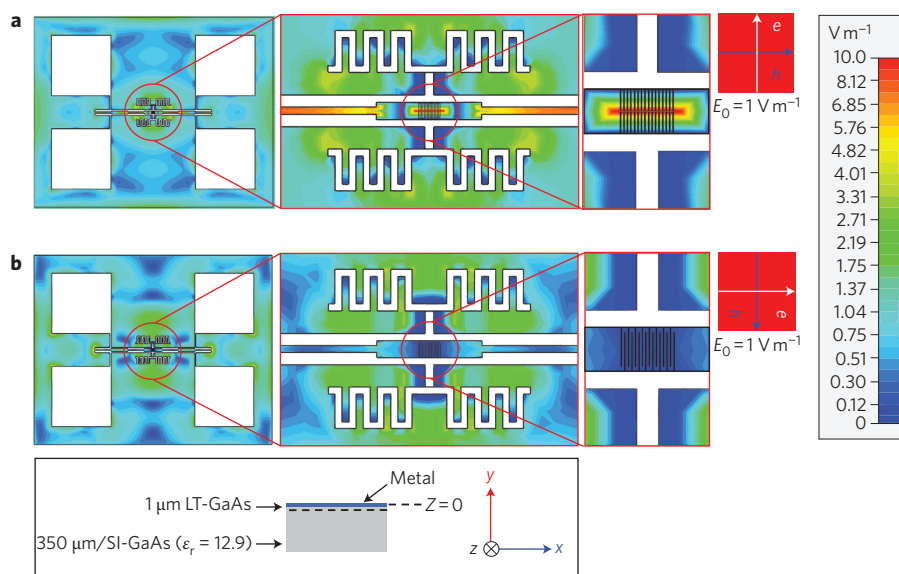

Figure 4 | Electric field amplitude in the near field of a modified meander antenna with different photomixers at 1 THz plane-wave illumination.
a, Photomixer with tip-to-tip nanogap electrodes. **b**, Photomixer with typical interdigitated electrodes. Inset: cross-sectional schematics of the devices and the axis convention used in the simulation.
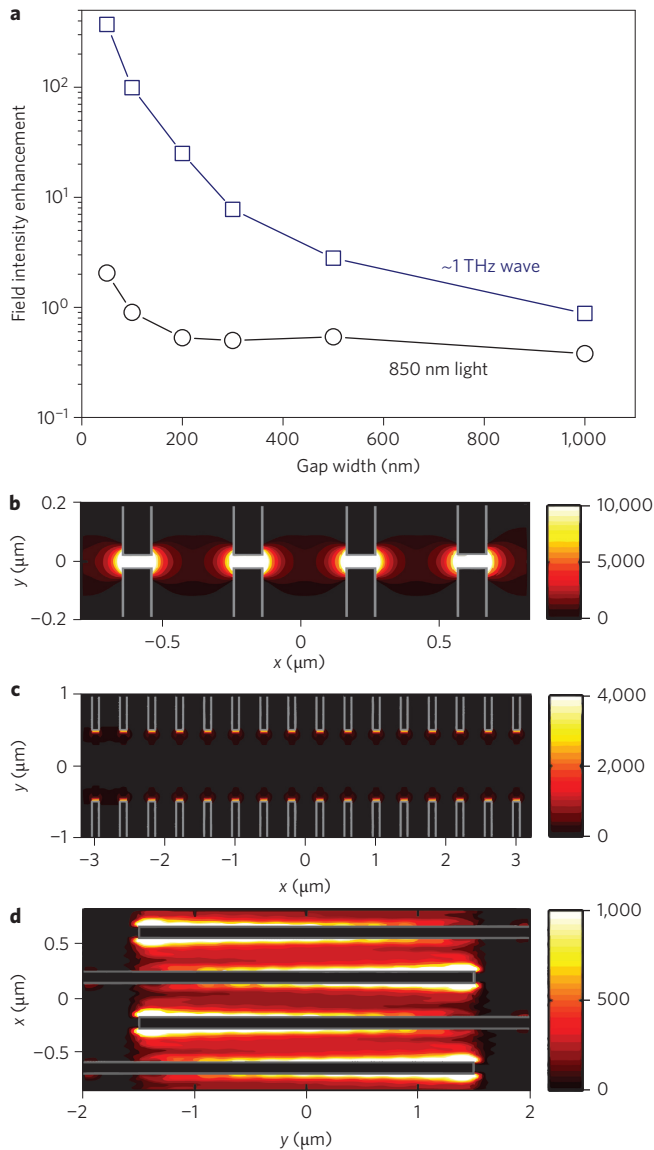
Figure 5 | FDTD simulation of electric field enhancement as a function of gap width and simulation of field intensity distributions within the active region under ∼1 THz plane-wave illumination. a, Electric field enhancement between the tip-to-tip nanogap electrode structures with varying gap width and typical interdigitated electrode structures. **b**, Electric field intensity distribution for tip-to-tip nanogap electrodes with 50 nm gap is greatly enhanced and concentrated within the gap. **c**, Electric-field intensity distribution for tip-to-tip nanogap electrodes with a 1,000 nm gap is concentrated at the tips of the electrodes. **d**, Electric-field intensity distribution for the interdigitated electrode configuration. The field at the tip of the electrodes is more intense than the field at the side surfaces of the electrodes.

pumping light, and found that the enhancement could be observed only when the gap was <100 nm. Figure 5b,c shows the electric field intensity distributions in the tip-to-tip nanogap electrode structures for 50 nm and 1,000 nm gaps, respectively. With the electric field component of the incident electromagnetic waves aligned in the y-direction, as the gap between two opposing electrodes narrows, the charge at the tip of opposing electrodes experiences a stronger attraction, subsequently inducing a greater accumulation of charges. The enhanced surface charge accumulations are the origin of the field enhancement shown in Fig. 5a. As the opposing electrodes are moved further apart, the attraction between surface

charges becomes weaker, and at 1,000 nm there is no enhancement within the gap and the field is only concentrated at the tip of electrodes, as shown in Fig. 5c.

In the case of the interdigitated electrodes structure, the field was also enhanced due to surface charge interaction. However, the strength of the enhancement was restricted by the width of the electrodes. This is because the surface charge density is limited by the total charge number per unit width of the electrode fingers as the electric field of the incident electromagnetic waves is aligned perpendicular to them. The surface charge density is therefore not as large as for the tip-to-tip nanogap electrodes with the electric field aligned along the length of the electrode fingers. Because the electrode width limits the surface charge, even if the separation between two electrode fingers is made smaller there will be no field enhancement as significant as for the tip-to-tip nanogap electrodes configuration. Furthermore, because of the broken symmetry in the y-axis of the interdigitated electrodes, part of the electric field component would deviate along this axis and induce charge flow along the length of the electrode fingers. These charges finally accumulate at the electrodes tips, and this accumulation results in a stronger field than that on the side surfaces of the electrodes.

The electric field distribution under the electrodes during d.c. bias was also different for the two configurations. In the case of the fabricated c.w. terahertz photomixer with tip-to-tip nanogap electrodes, the E-field intensity within the 100 nm gap was enhanced by a factor of at least three due to the smaller separation between opposing electrodes compared to the device with typical interdigitated electrodes with a separation of 300 nm. Edge effects also have an impact on the distributions of the electric field, with a significant increment in charge collection ability at the edge of the electrodes. This improves the near-anode photogenerated-carrier capture mechanism at the electrodes, increasing both the d.c. and terahertz photocurrent.

We also investigated the effect of the meander antenna structures on the characteristics of the photomixers. For both tip-to-tip nanogap and interdigitated electrodes, the active region can be regarded as a capacitor-like terahertz current source. It can be modelled in CST Microwave Studio as a discrete current source used to excite the meander antenna. The region between the electrodes and bias pads has a choke acting as a filter to minimize the flow of radio-frequency (RF) currents into the bias lines to avoid unwanted radiation. The meander structure acts to inductively load the dipole to compensate the capacitor-like active source to achieve better impedance matching, and shifts the resonance frequency down to ∼0.5 THz. The electrodes in the active region further enlarge the effective dipole length and have similar effects in shifting the antenna resonant frequency down to ∼0.4 THz for tip-to-tip nanogap electrodes, as can be observed in Fig. 3b. In the case of interdigitated electrodes, because of the longer electrodes, the resonant frequency is shifted even lower. This lower resonant frequency leads to a smaller efficiency at higher terahertz frequencies for the photomixer with interdigitated electrodes, contributing to its smaller bandwidth compared to the photomixer with tip-to-tip nanogap electrodes. Furthermore, the simulation confirms that the tip-to-tip nanogap electrode has a much smaller capacitance than interdigitated electrodes, while having better impedance matching to the meander antenna. When we consider the equivalent circuit of a terahertz photomixer in which it is simplified as capacitance and resistance, the relationship between the terahertz output power and the circuit capacitance is given by[18]

$$P_{\mathrm{THz}}(\omega) \propto \frac{1}{1 + (\omega R_{\mathrm{A}} C)^2} \qquad (1)$$

where P_{THz} is the mean power of the terahertz output, ω is the frequency, R_{A} is the antenna resistance, and C is the capacitance of the photomixer. Using COMSOL, we calculated the capacitance

of the nanogap electrode antenna structure to be 2.1 fF and that of the interdigitated structure to be 3.2 fF. This translates to a factor of at least 2.3 enhancement of P_{THz}. A lower RC time constant also allows for better output power performance, especially at the higher part of the terahertz spectrum.

In summary, a highly efficient c.w. terahertz source using nano-electrodes in the active region of the photomixer is demonstrated. Full-field electromagnetic simulations reveal that the photomixer active region with tip-to-tip nanogap electrodes actively radiates terahertz waves, in contrast to the active region with typical interdigitated electrodes. FDTD simulations show two orders of magnitude field enhancements in the terahertz region in the tip-to-tip nanogap electrodes with a 100 nm gap when compared to the interdigitated electrodes configuration. With the E-field of the impinging electromagnetic waves polarized parallel to the opposing electrodes, the enhanced terahertz field leads to a stronger force driving the photogenerated carriers to the electrodes more efficiently. The new active region structure also provides good impedance matching to the terahertz planar antenna and exhibits a lower RC time constant, allowing more efficient radiation, particularly at the higher part of the terahertz spectrum. Measurement results from the fabricated photomixers show about two orders of magnitude output power enhancement and about two times larger bandwidth in the c.w. terahertz photomixer with the tip-to-tip nanogap active region than that with conventional interdigitated electrodes.

Methods

The investigated devices consisted of 1 µm LT GaAs and a 1 µm AlAs heat-spreading layer grown on a semi-insulating GaAs substrate using solid-source MBE. The growth temperature for LT GaAs was ∼300 °C with in situ post-growth annealing at 600 °C for 10 min. Hall effect measurements revealed a resistivity of ∼5 × 10⁷ Ω cm and room-temperature carrier mobility of ∼5,000 cm² V⁻¹ s⁻¹. This is similar to observations of the Hall effect for intrinsic GaAs materials[37]. The carrier lifetime of the LT GaAs was found to be <1 ps. As for LT GaAs, the effects of As precipitates are noted for their unique electrical properties.

A modified meander antenna was adopted for the c.w. terahertz photomixer. The meander antenna was patterned using a standard photolithography and metal lift-off process. The LT-GaAs wafer was first cleaned with acetone and methanol (5 min each) and rinsed with deionized (DI) water. The wafer was then baked in an oven at 120 °C for 10 min for dehydration. This was followed by AZ5214 photoresist-coating with a spin speed of 5,000 r.p.m. and a soft bake at 90 °C for 90 s. Photolithography was carried out using a mask aligner SUSS MicroTec (MA8/BA6). Layers of titanium and gold (10 nm and 150 nm, respectively) were deposited using a Denton Explorer electron-beam evaporator and ultrasonic-assisted lift-off to form the PCA. To define the submicrometre electrodes, the patterned wafers were coated with poly(methyl methacrylate) (PMMA) with a spin speed of 3,000 r.p.m. The soft bake was carried out at 180 °C for 10 min. The interdigitated electrodes pattern and nanogap electrode pattern without opening of the central gap were formed by electron-beam lithography on PMMA using an Elionix ELS-7000 electron-beam lithography system at a current of 100 pA and dose time of 2.4 µs/dot. The patterns were developed using methyl isobutyl ketone : isopropyl alcohol (1:3). Titanium and gold layers (5 nm and 100 nm, respectively) were deposited by electron-beam evaporation and a lift-off process. The connected nanogap electrodes were finally separated by focused ion beam milling using an FEIFIB 200XP single-beam FIB at 70 pA current.

The wafers were then diced and mounted on a hyper-hemispherical lens made of high-resistivity silicon (Batop GmbH). The electrode active region, also the pumping light illumination area, had an area of ∼5 µm × 8 µm. Voltage biasing of the device was achieved using probes attached to a Keithley source meter, which also functioned as a photocurrent meter. Two tunable c.w. single-frequency semiconductor lasers (Toptica DFB) operating at central wavelengths of 852 nm and 855 nm were used as the excitation light source. The two laser beams were combined using a 2 × 1 single-mode polarization-maintaining fibre. After amplification at a Toptica BoosTA semiconductor amplifier, the fibre-coupled combined laser beam was aligned to the photomixer active region using a Newport XYZ micrometre precision stage. The tuning of the laser frequency offset was conducted by carefully setting the two laser temperatures at a calibrated temperature. At each frequency offset point, the emission spectra from the photomixer were obtained using FTIR in conjunction with a liquid-helium-cooled silicon bolometer. The characteristic of the photomixer emission was its narrow linewidth, as determined by the laser pump source. In our case, the laser linewidth was <10 MHz. The recorded emission spectra linewidth was limited by the resolution of the FTIR system (∼6 GHz).

A schematic of the measurement set-up is shown in Supplementary Fig. 1. Each photomixer was mounted on a dedicated stage with bias probes and placed directly in front of the FTIR input window. For data collection, the FTIR scanning range was

set between 5 and 70 cm⁻¹, where 1 THz ≈ 33.33 cm⁻¹. The acquisition mode used was single-sided forward–backward, with a scanning resolution of 0.2 cm⁻¹. A Mylar 50 µm beamsplitter was used. To obtain the output power of the photomixers, we first calibrated the bolometer intensity reading using a standard mercury lamp supplied with the FTIR system. Such a lamp has been characterized to behave as an ideal blackbody source at 4,000 K at a frequency less than 2 THz. Placing the lamp at the same position as the photomixer, the spectra of the lamp was obtained using the FTIR with the bolometer detector. The radiated power of a blackbody source within a particular wavelength range could then be calculated using the following approximation[38]:

$$\Delta P = \frac{2\pi hc^2}{\lambda^5} \frac{1}{e^{hc/\lambda kT} - 1} \Delta \lambda A \qquad (2)$$

where h is Planck's constant, c is the speed of light, T is absolute temperature, λ is the wavelength, and A is the light source area, which in this case was determined by the size of the aperture on an aperture disk in the FTIR system (Supplementary Fig. 1). Here, the aperture diameter was fixed at 8 mm. The spectra of the photomixers could then be compared with the reference spectra of the mercury lamp. By comparing the integrated intensity of the photomixer emission spectrum and the mercury-lamp spectrum at a particular frequency range and referring to the calculated blackbody power, the output power of the c.w. terahertz photomixers could be obtained.

References

1. Winnewisser, G. Spectroscopy in the terahertz region. *Vibrat. Spectrosc.* **8,** 241–253 (1995).
2. Siegel, P. H. Terahertz technology. *IEEE Trans. Microw. Theory Tech.* **50,** 910–928 (2002).
3. Hu, B. B. & Nuss, M. C. Imaging with terahertz waves. *Opt. Lett.* **20,** 1716–1718 (1995).
4. Shen, Y. C. *et al.* Detection and identification of explosives using terahertz pulsed spectroscopic imaging. *Appl. Phys. Lett.* **86,** 241116 (2005).
5. Tonouchi, M. Cutting-edge terahertz technology. *Nature Photon.* **1,** 97–105 (2007).
6. Williams, B. S. Terahertz quantum-cascade lasers. *Nature Photon.* **1,** 517–525 (2007).
7. Qin, Q., Williams, B. S., Kumar, S., Hu, Q. & Reno, J. L. Tuning a terahertz wire laser. *Nature Photon.* **3,** 732–737 (2009).
8. Amanti, M. I., Fischer, M., Scalari, G., Beck, M. & Faist, J. Low-divergence single-mode terahertz quantum cascade laser. *Nature Photon.* **3,** 586–590 (2009).
9. Kumar, S. Chan, C. W. I., Hu, Q. & Reno, J. L. A 1.8-THz quantum cascade laser operating significantly above the temperature of $\hbar\omega/k_B$. *Nature Phys.* **7,** 166–171 (2011).
10. Maineult, W. *et al.* Metal–metal terahertz quantum cascade laser with micro-transverse-electromagnetic-horn antenna. *Appl. Phys. Lett.* **93,** 183508 (2008).
11. Kumar, S., Hu, Q. & Reno, J. L. 186 K operation of terahertz quantum-cascade lasers based on a diagonal design. *Appl. Phys. Lett.* **94,** 131105 (2009).
12. Ferguson, B. & Zhang, X. C. Materials for terahertz science and technology. *Nature Mater.* **1,** 26–33 (2002).
13. Preu, S., Döhler, G. H., Malzer, S., Wang, L. J. & Gossard, A. C. Tunable, continuous-wave terahertz photomixer sources and applications. *J. Appl. Phys.* **109,** 061301 (2011).
14. McIntosh, K. A. *et al.* Terahertz photomixing with diode lasers in low-temperature-grown GaAs. *Appl. Phys. Lett.* **67,** 3844–3846 (1995).
15. Gregory, I. S. *et al.* Resonant dipole antennas for continuous-wave terahertz photomixers. *Appl. Phys. Lett.* **85,** 1622–1624 (2004).
16. Brown, E. R., McIntosh, K. A., Nichols, K. B. & Dennis, C. L. Photomixing up to 3.8 THz in low-temperature-grown GaAs. *Appl. Phys. Lett.* **66,** 285–287 (1995).
17. Brown, E. R. THz generation by photomixing in ultrafast photoconductors. *Int. J. High Speed Electron. Syst.* **13,** 497–545 (2003).
18. Gregory, I. S. *et al.* Optimization of photomixers and antennas for continuous-wave terahertz emission. *IEEE J. Quant. Electron.* **41,** 717–728 (2005).
19. Duffy, S. M. *et al.* Accurate modeling of dual dipole and slot elements used with photomixers for coherent terahertz output power. *IEEE Trans. Microwave Theor. Tech.* **49,** 1032–1038 (2001).
20. Mangeney, J. *et al.* Continuous wave terahertz generation up to 2 THz by photomixing on ion-irradiated In$_{0.53}$Ga$_{0.47}$As at 1.55 µm wavelengths. *Appl. Phys. Lett.* **91,** 241102 (2007).
21. Samir, R. *et al.* Enhanced terahertz emission from a multilayered low temperature grown GaAs structure. *Appl. Phys. Lett.* **96,** 091101 (2010).
22. Sartorius, B. *et al.* Continuous wave terahertz systems exploiting 1.5 µm telecom technologies. *Opt. Express* **17,** 15001–15007 (2009).
23. Mikulics, M., Marso, M., Lepsa, M., Grützmacher, D. & Kordo, P. Output power improvement in MSM photomixers by modified finger contacts configuration. *IEEE Photon. Tech. Lett.* **21,** 146–148 (2009).

24. Pendry, J. B., Martin-Moreno, L. & Garcia-Vidal, F. J. Mimicking surface plasmons with structured surfaces. *Science* **305,** 847–848 (2004).
25. Williams, C. R. *et al.* Highly confined guiding of terahertz surface plasmon polaritons on structured metal surfaces. *Nature Photon.* **2,** 175–179 (2008).
26. Williams, C. R. *et al.* Dual band terahertz waveguiding on a planar metal surface patterned with annular holes. *Appl. Phys. Lett.* **96,** 011101 (2010).
27. Chen, H. T. *et al.* Experimental demonstration of frequency-agile terahertz metamaterials. *Nature Photon.* **2,** 295–298 (2008).
28. Chen, H. T. *et al.* A metamaterial solid-state terahertz phase modulator. *Nature Photon.* **3,** 148–151 (2009).
29. Landy, N. I., Sajuyigbe, S., Mock, J. J., Smith, D. R. & Padilla, W. J. Perfect metamaterial absorber. *Phys. Rev. Lett.* **100,** 207402 (2008).
30. Yu, N. *et al.* Designer spoof surface plasmon structures collimate terahertz laser beams. *Nature Mater.* **9,** 730–735 (2010).
31. Seo, M. A. *et al.* Terahertz field enhancement by a metallic nano slit operating beyond the skin-depth limit. *Nature Photon.* **3,** 152–156 (2009).
32. Novotny, L. & Hecht, B. *Principles of Nano-optics* (Cambridge Univ. Press, 2007).
33. Kawano, Y. & Ishibashi, K. An on-chip near-field terahertz probe and detector. *Nature Photon.* **2,** 618–621 (2008).
34. Chen, H-T. *et al.* Active terahertz metamaterials devices. *Nature* **444,** 597–600 (2006).
35. Large, N., Abb, M., Aizpurua, J. & Muskens, O. L. Photoconductively loaded plasmonic nanoantenna as building block for ultracompact optical switches. *Nano Lett.* **10,** 1741–1746 (2010).
36. Mühlschlegel, P., Eisler, H. J., Martin, O. J., Hecht, B. & Pohl, D. W. Resonant optical antennas. *Science* **308,** 1607–1609 (2005).
37. Orton, J. *The story of Semiconductors* (Oxford Univ. Press, 2004).
38. Widger, W. K. Jr & Woodall, M. P. Integration of the Planck blackbody radiation function. *Bull. Am. Meteorol. Soc.* **57,** 1217–1219 (1976).

Author contributions

J.H.T. conceived the idea and supervised the project. H.T. and Q.Y.W. contributed to the fabrication and characterization of the c.w. terahertz photomixer. M.S., Z.N.C., S.A.M. and B.W. contributed to the theory and simulation. H.T. and S.J.C. contributed to the wafer growth. C.C.C., S.G.Y. and A.J.D. contributed to the nanofabrications. H.T., J.H.T., B.W., M.S. and S.A.M. contributed to writing the manuscript. All authors discussed the results and contributed to the article.

Additional information

The authors declare no competing financial interests. Supplementary information accompanies this paper at www.nature.com/naturephotonics. Reprints and permission information is available online at http://www.nature.com/reprints. Correspondence and requests for materials should be addressed to J.H.T.